Available online at www.sciencedirect.com
SCIENCE DIRECT®
ELSEVIER
Journal of Nuclear Materials 322 (2003) 91–97
journal of nuclear materials
www.elsevier.com/locate/jnucmat

Correlation between characteristics of grain boundary carbides and creep–fatigue properties in AISI 321 stainless steel

Kyung Seon Min, Soo Woo Nam *

Department of Materials Science and Engineering, Korea Advanced Institute of Science and Technology, 373-1 Guseong-dong, Yuseong-gu, Daejeon 305-701, South Korea

Received 20 December 2002; accepted 1 May 2003

Abstract

The effects of the interfacial relationships between grain boundary carbides and neighboring grains on the creep–fatigue behaviors have been investigated in AISI 321 stainless steel. The contacting interfacial planes between grain boundary TiC and neighboring grains are found to have lower Miller indices than those between $Cr_{23}C_6$ and neighboring grains. From this observation, it is suggested that the interfacial free energy between grain boundary TiC and grains is lower than that between $Cr_{23}C_6$ and grains. Creep–fatigue life of TiC aged AISI 321 stainless steel is observed to be longer than that of $Cr_{23}C_6$ aged AISI 321 stainless steel. The differences in creep–fatigue life are based on the stronger cavitation resistance of TiC compared with that of $Cr_{23}C_6$. From the interfacial relationships between the grain boundary carbides and the neighboring grains, it is verified that formation and growth of grain boundary cavities at TiC carbides are more retarded than those at $Cr_{23}C_6$ carbides, thus extending the creep–fatigue life of the steel.
© 2003 Elsevier B.V. All rights reserved.

PACS: 81.40.Cd; 62.20.Mk; 68.35.Md; 68.37.Lp

1. Introduction

AISI 321 stainless steel has been widely used in the power-generation industry because it has good corrosion resistance through inhibited grain boundary sensitization [1–3]. This alloy is used mainly in superheater tubing in conventional coal-fired boilers, as well as other critical applications such as guide tubes, pipes, and pressure vessels in gas-cooled nuclear reactors. The addition of Ti prevents the formation of chromium-rich carbide precipitates in the grain boundaries which are known to be deleterious to the creep life of the alloy [4–6].

Particularly in austenitic stainless steels, grain boundary cavitation is the most serious detrimental process in degradation under creep–fatigue interaction conditions [7–11]. Carbide at the grain boundary provides a preferential site for cavity nucleation under creep–fatigue interaction conditions, reducing the creep–fatigue life drastically. Thus, it can be inferred that carbide distribution, carbide morphology and carbide interfacial free energy are important factors in determining creep–fatigue resistance of austenitic stainless steels [9–12].

Earlier research on grain boundary carbides concentrated on the improvement of corrosion resistance in AISI 321 stainless steels [1–3]. Although there have been reports on the mechanical properties of steel aged with TiC, which is the main precipitate in AISI 321 stainless steels, these studies only illustrated the mechanical properties of $Cr_{23}C_6$ aged alloys [7–14].

It is very important to understand the characteristics of grain boundary carbides in austenitic stainless steels, because the carbides become the grain boundary cavitation sites under creep condition.

* Corresponding author. Tel.: +82-42 869 3318; fax: +82-42 869 3310.
E-mail address: namsw@cais.kaist.ac.kr (S.W. Nam).

0022-3115/$ - see front matter © 2003 Elsevier B.V. All rights reserved.
doi:10.1016/S0022-3115(03)00274-5

The purpose of this paper is to investigate the characteristics of TiC and $Cr_{23}C_6$ carbides precipitated at the grain boundary and the correlation between the interfacial properties of the two carbides (TiC and $Cr_{23}C_6$) and the creep–fatigue properties of AISI 321 stainless steel. Creep–fatigue tests are conducted using specimens with TiC carbide, which is the main carbide, and with $Cr_{23}C_6$ carbide, which is precipitated as a reference for comparison with the effects of TiC carbide in AISI 321 stainless steel.

2. Experimental procedures

The chemical composition and heat treatment conditions of the investigated AISI 321 stainless steel are shown in Table 1. After solution heat treatments, two different aging treatment processes are designed to independently form TiC and $Cr_{23}C_6$ carbides at the grain boundary. Even though the particles of TiC and $Cr_{23}C_6$ have similar size and density at the grain boundary, the different lattice parameters and different interfacial energies of the two carbides could uniquely affect the cavitation resistance of the alloys. To obtain TiC and $Cr_{23}C_6$ with similar size and density at grain boundaries, the following two different heat treatment processes were applied. For TiC carbide precipitation, after solid solution treatment at 1373 K for 0.5 h, the alloy was furnace-cooled to 1203 K and held for 10 h followed by water quenching. And for $Cr_{23}C_6$ carbide precipitation, after solid solution treatment at 1373 K for 0.5 h, the alloy was water quenched and then aged for 24 h at 1023 K.

In order to investigate the crystallographic relationship of the carbides with respect to the matrix, TEM foils were used. TEM foils were prepared by the twin-jet method using 5 vol.% perchloric acid + 95 vol.% acetic acid at 288 K and 30 V. The grain boundary plane normal was obtained by the cross product of at least two beam directions to which the carbide plane and grain boundary plane are parallel. In this situation, that is, with the narrowest boundary area, the grain boundary could be seen as a line and was fully covered by precipitates. The approximate orientation of the incoherent carbide interface could be obtained by using the trace analysis method, which has been previously used for other alloy systems [15]. The interfacial planes between grain boundary carbides and the matrix were obtained by a high resolution transmission electron microscope (HRTEM) Philips Technai F20 operating at 200 kV.

Total strain controlled low cycle fatigue tests with 0.5 h tensile hold time at the maximum tensile strain were conducted at 873 K with a total strain range ($\Delta\varepsilon_t$) of ±1.0 to ±2.0%. The critical number of cycles to failure, N_{cr}, defined as the number of fatigue cycles leading to a 20% reduction of the saturated tensile peak load [16], was used to measure the fatigue life.

In order to observe grain boundary carbides and cavities, the tested specimens were chilled in liquid nitrogen temperature (LNT) and subsequently broken by impact along the most damaged and weakest parts and then examined with a Jeol 840A scanning electron microscope (SEM).

3. Results and discussion

3.1. Carbide distribution and morphology of TiC and $Cr_{23}C_6$ at grain boundary

Fig. 1 shows the carbide distributions and morphologies of TiC and $Cr_{23}C_6$ at grain boundaries after the heat treatments. In Fig. 1(a), it is observed that TiC particles are precipitated at grain boundaries and the size of the TiC particles is about 1–3 μm. The precipitates of $Cr_{23}C_6$, having similar size as TiC, are also precipitated at the grain boundaries as shown in Fig. 1(b). The morphologies of TiC and $Cr_{23}C_6$ are observed to be planar along the grain boundaries.

To quantify the density of the grain boundary carbides, the linear density of the carbides was measured by an image analyzer with SEM micrographs. The measured densities of the TiC and $Cr_{23}C_6$ carbides were similar, 1.11×10^5 and 1.18×10^5/m, respectively.

TEM micrographs showing the carbide morphologies of TiC and $Cr_{23}C_6$ at the grain boundaries are provided in Fig. 1(c) and (d), respectively. It is observed that the shape of the $Cr_{23}C_6$ carbide resembles a plate growing into a grain, while the other side of the carbide maintains a flat interface with the grain boundary. It is well known that in relation to these phenomena, precipitation accompanies the best possible registry in order to minimize the interfacial energy of the precipitate facet [17,18]. However, TiC has a planar shape penetrating

Table 1
The chemical composition and the heat treatment conditions for AISI 321 stainless steel (all in wt%)

C	Ti	Si	Mn	P	S	Cr	Ni	Mo	Cu	N
0.03	0.257	0.602	1.44	0.024	0.002	17.90	9.15	0.096	0.198	0.012

Aging heat treatments for TiC and $Cr_{23}C_6$ after solution treatments.
(1) TiC aged: Solution treatment (1373 K/0.5 h) → Furnace cooled to 1203 K → Aging treatment (1203 K/10 h/WQ).
(2) $Cr_{23}C_6$ aged: Solution treatment (1373 K/0.5 h/WQ) → Aging treatment (1023 K/24 h/WQ).

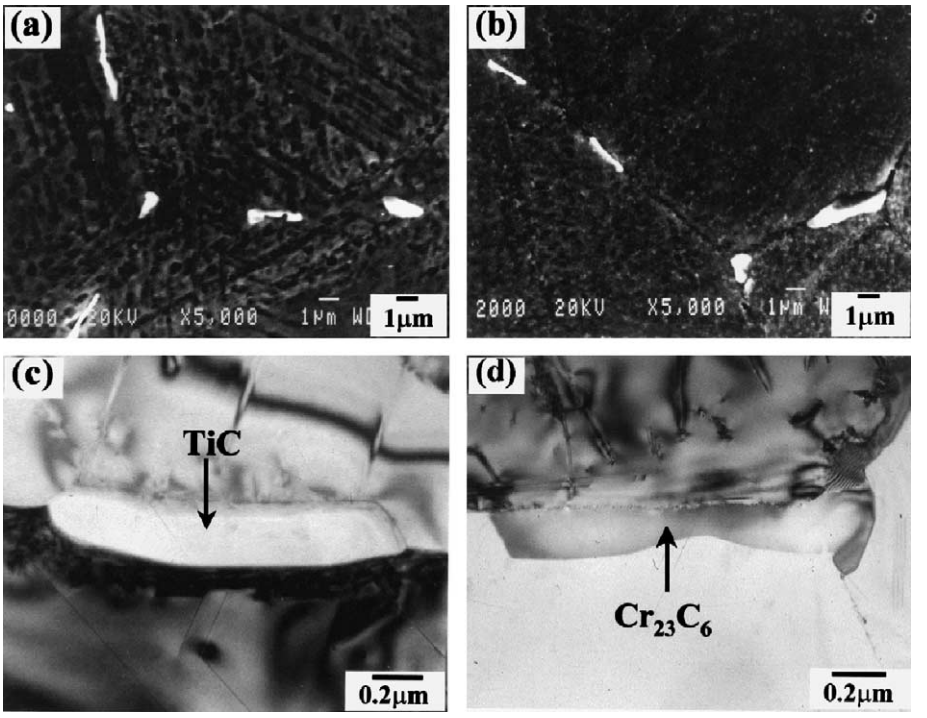

Fig. 1. Micrographs showing the carbide distribution and morphology of TiC and $Cr_{23}C_6$ at grain boundaries: (a) SEM micrograph of TiC, (b) SEM micrograph of $Cr_{23}C_6$, (c) TEM micrograph of TiC and (d) TEM micrograph of $Cr_{23}C_6$.

the grain boundary, but both sides of the carbide are growing into each neighboring grains.

3.2. Crystallographic analysis of TiC and $Cr_{23}C_6$ at the grain boundaries

In order to investigate the difference in growth directions with different carbide types, HRTEM imaging was used, as shown in Fig. 2. An HR image for a flat interface between TiC and one grain at the grain boundary is shown in Fig. 2(a). When the beam direction for TiC is [0 1 1], it is clearly shown that the TiC shares a coherency with grain 1 and the orientation relationship is revealed to be $(1\,1\,\bar{1})_{TiC}\|(1\,1\,\bar{1})_{G1}$ (G1 indicates grain 1). On the other hand, because no lattice image is observed in grain 2 as shown in Fig. 2(b), the interface relationship between the TiC and grain 2 with the same beam direction is incoherent.

For comparison with the results of the TiC carbides, the HRTEM for $Cr_{23}C_6$ and a neighboring grain at the grain boundary is observed, as shown in Fig. 3(a). When the beam direction for $Cr_{23}C_6$ is [0 1 1], $Cr_{23}C_6$ and one of the neighboring grains (grain 1) have a coherent plane of $(1\,1\,\bar{1})_{Cr_{23}C_6}\|(1\,1\,\bar{1})_{G1}$. In Fig. 3(b), the plane of $Cr_{23}C_6$ at the incoherent interface between $Cr_{23}C_6$ and grain 2 was observed to be parallel to the coherent interface, i.e. $(1\,1\,\bar{1})_{Cr_{23}C_6}$. From these observations, it is supposed that the interface indices of TiC and $Cr_{23}C_6$ carbides at the grain boundary are always identified as low and rational. This is consistent with findings reported in other literature where the low and rational indices of interfaces were associated with a low energy interface to reduce their total surface energy [14,18,19]. However, since it is difficult to observe the indices of incoherent planes of the grains with HRTEM, trace analysis is employed instead [14,15].

Trace analyses were used to determine the respective orientations of the grain boundary planes for each grain, and in particular the orientation of the incoherent planes. In Fig. 4(a), the beam direction for TiC is [0 1 1] and orientation results are obtained by tilting the foil to the orientation in which the flat broad planes of TiC were parallel to the beam direction with the smallest carbide area. When the misorientation axis/angle of TiC and grain 1 is determined to be $[\bar{2}, 0.3, \overline{1.7}]/22.9°$, it is revealed that the broad planes between TiC and grain 1 are $(1\,1\,\bar{1})_{TiC}/(1\,3\,\bar{1})_{G1}$. The misorientation axis/angle of TiC and grain 2 is determined to be [1.2, 0.7, 1.9]/73.4° and the indices of the broad planes of TiC and grain 2 are $(1\,1\,\bar{1})_{TiC}/(3\,3\,\bar{1})_{G2}$, respectively.

As already shown in Fig. 3(a) of HRTEM, the interfacial planes between $Cr_{23}C_6$ and grain 1 are $(1\,1\,\bar{1})_{Cr_{23}C_6}/(1\,1\,\bar{1})_{G1}$. In this case, beam directions represent [0 1 1] and $[0.31, \overline{0.35}, 0.94]$ for grains 1 and 2,

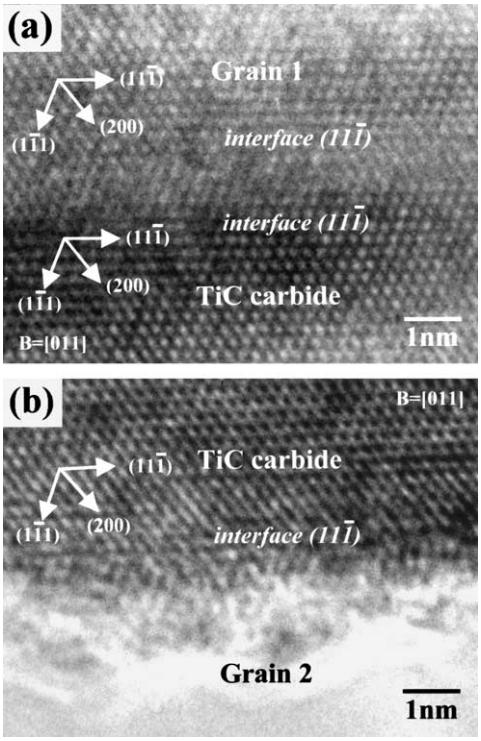

Fig. 2. HRTEM micrographs showing the interfaces of TiC and neighboring grain at grain boundary: (a) coherent interface and (b) incoherent interface.

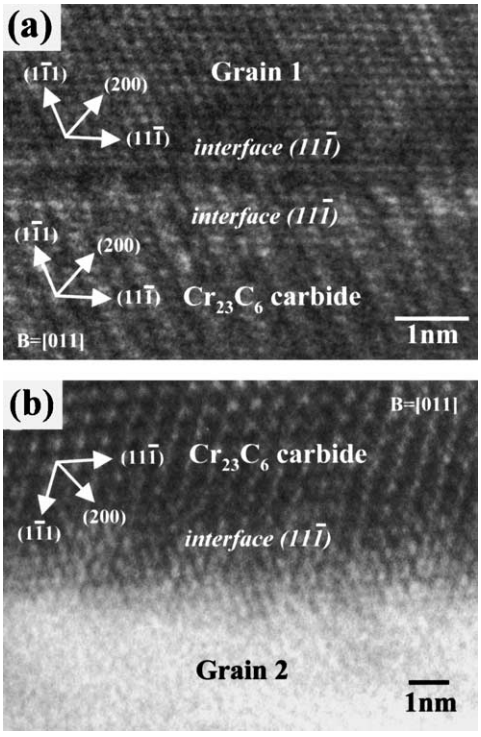

Fig. 3. HRTEM micrographs showing the interfaces of $Cr_{23}C_6$ and neighboring grain at grain boundary: (a) coherent interface and (b) incoherent interface.

respectively, as shown in Fig. 4(b). These planes have a precisely coherent relationship between $Cr_{23}C_6$ and grain 1. However the incoherent planes between $Cr_{23}C_6$ and grain 2 are $(1\,1\,\bar{1})_{Cr_{23}C_6}/(8\,4\,\bar{2})_{G2}$. From these misorientation values between carbides and neighboring grains, those between TiC and neighboring grains are lower index planes to decrease the interfacial energy than those between $Cr_{23}C_6$ and neighboring grains.

Possible interfaces between carbides and neighboring grains at incoherent interfaces are calculated to clarify these relationships in Tables 2 and 3. In Table 2, $(1\,1\,\bar{1})$ of TiC has a smaller misorientation angle with $(3\,3\,\bar{1})$ of grain 2 than the other low indices planes of the carbide. So the observed results are in concordance with the calculation results, it seems reasonable that this interface relationship is determined by plane matching. As it is shown in Table 3, $(1\,1\,\bar{1})$ of $Cr_{23}C_6$ has a smaller misorientation angle with $(8\,4\,\bar{2})$ of grain 2 than with other planes of $Cr_{23}C_6$.

In addition, further plane relationships between carbides and neighboring grains of several carbides at incoherent interfaces are summarized in Table 4. From these results, indices of the incoherent interface planes of TiC and neighboring grains are found to be lower than those of $Cr_{23}C_6$ and neighboring grains. On the basis of these observations, it may be supposed that the interfacial free energy between TiC and the matrix is lower than that between $Cr_{23}C_6$ and the matrix for the incoherent interfacial relationships between carbides and neighboring matrix.

Meanwhile, the morphologies of carbides exhibit a polyhedral rather than rectangular shape at the grain boundary edge, as shown in Fig. 4. From an interfacial free energy point of view, the morphology of carbides was schematically drawn for both TiC and $Cr_{23}C_6$ carbides. If the morphology of TiC has rectangular shape at grain boundary edge, as shown in Fig. 5(a), the interfacial plane of TiC at the perpendicular part is $(4\,\bar{2}\,2)$. When TiC has a hexagonal shape, as shown in Fig. 5(b), the inclined interfacial planes of TiC are $(1\,\bar{1}\,1)$ or $(2\,0\,0)$ at the grain boundary. Having this shape, although the interfacial area is increased, the total interfacial free energy of the inclined boundary would be lower than for the interface shown in Fig. 5(a) since the interfacial free energy per unit area would be decreased.

If the morphology of $Cr_{23}C_6$ has a perpendicular shape at the grain boundary edge, the interfacial plane of $Cr_{23}C_6$ is also $(4\,\bar{2}\,2)$ as shown in Fig. 6(a). However, when $Cr_{23}C_6$ has a quadrilateral shape, as shown in Fig. 6(b), the inclined interfacial planes of $Cr_{23}C_6$ are $(1\,\bar{1}\,1)$ or $(2\,0\,0)$ at the interface.

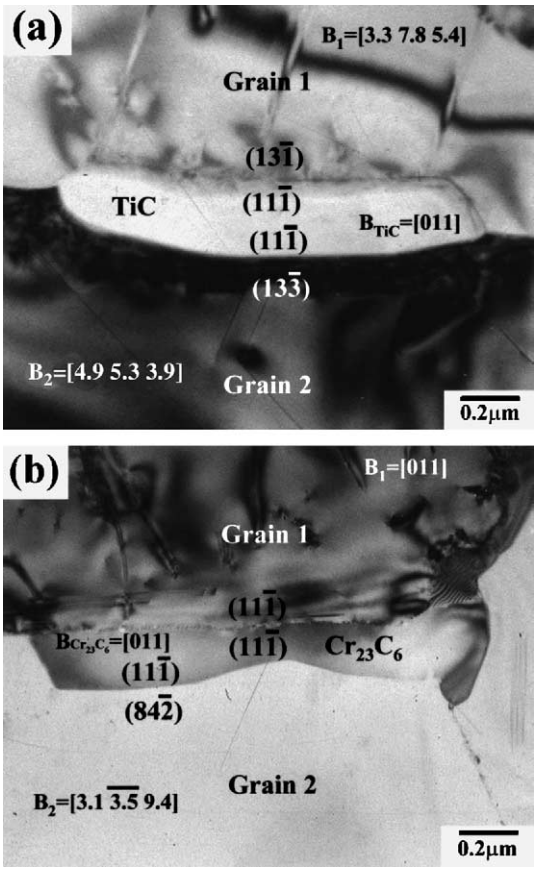

Fig. 4. TEM micrograph showing the interfacial planes of carbides and neighboring grains: (a) TiC and (b) $Cr_{23}C_6$.

Table 2
Crystallographic features between TiC and grain 2 in Fig. 4(a)

Possible incoherent interfacial planes of TiC	Misorientation angle between TiC and (3 3 $\bar{1}$)	Order of possibility to be interface of TiC
(1 1 $\bar{1}$)	22.0°	1
(1 $\bar{1}$ 1)	82.4°	4
(2 0 0)	46.5°	2
(0 2 $\bar{2}$)	49.5°	3

Table 3
Crystallographic features between $Cr_{23}C_6$ and grain 2 in Fig. 4(b)

Possible incoherent interfacial planes of $Cr_{23}C_6$	Misorientation angle between $Cr_{23}C_6$ and (8 4 $\bar{2}$)	Order of possibility to be interface of $Cr_{23}C_6$
(1 1 $\bar{1}$)	28.1°	1
(1 $\bar{1}$ 1)	82.8°	4
(2 0 0)	29.2°	2
(0 2 $\bar{2}$)	62.4°	3

Table 4
Crystallographic features between grain boundary carbides and neighboring grains

Carbide type	TiC	$Cr_{23}C_6$
Interfacial planes between carbides and grain 1	(1 1 $\bar{1}$)/(1 3 $\bar{1}$) (1 1 $\bar{1}$)/(3 3 $\bar{1}$) (1 1 $\bar{1}$)/(5 1 $\bar{1}$)	(1 1 $\bar{1}$)/(1 1 $\bar{1}$) (1 1 $\bar{1}$)/(1 1 $\bar{1}$) (1 1 $\bar{1}$)/(1 1 $\bar{1}$)
Interfacial planes between carbides and grain 2	(1 1 $\bar{1}$)/(3 3 $\bar{1}$) (1 1 $\bar{1}$)/(5 3 $\bar{1}$) (1 1 $\bar{1}$)/(5 5 $\bar{3}$)	(1 1 $\bar{1}$)/(8 4 $\bar{2}$) (1 1 $\bar{1}$)/(10,6,$\bar{4}$) (1 1 $\bar{1}$)/(14,6,$\bar{8}$)
Relative indices of incoherent interfacial planes	Lower	Higher

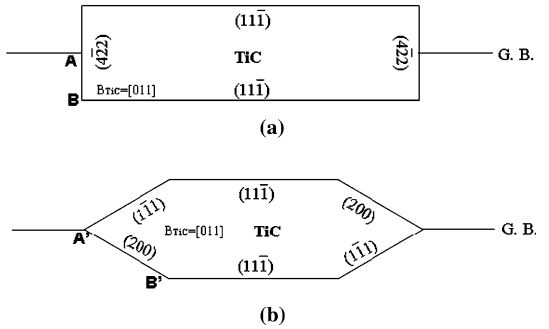

Fig. 5. Schematic diagram showing the crystallography and morphology of TiC at grain boundary: (a) when TiC has rectangular shape and (b) when TiC has hexagonal shape.

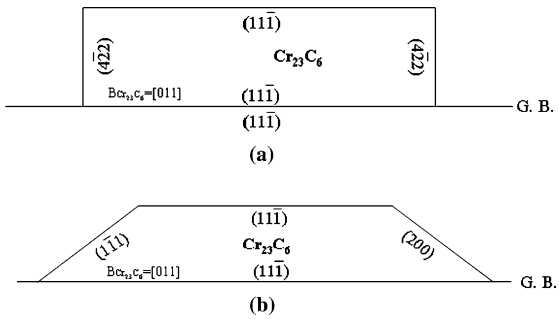

Fig. 6. Schematic diagram showing the crystallography and morphology of $Cr_{23}C_6$ at grain boundary: (a) when $Cr_{23}C_6$ has rectangular shape and (b) when $Cr_{23}C_6$ has quadrilateral shape.

From these results, regardless of carbide types (TiC and $Cr_{23}C_6$), the morphology of the carbide edge at the grain boundary formed in a polyhedral rather than rectangular shape to reduce the interfacial free energy per unit area. This investigation indicates that carbide morphology is determined by the minimization of the interfacial free energy per unit area during the carbide growth.

3.3. Comparison of the creep–fatigue behaviors with different grain boundary carbides

Fig. 7 shows the Coffin–Manson plots of the creep–fatigue tests. Although the two carbide densities at grain boundaries are similar, the plots indicate that the creep–fatigue life of TiC aged alloy is 40% longer than that of $Cr_{23}C_6$ aged alloy at the same total strain range.

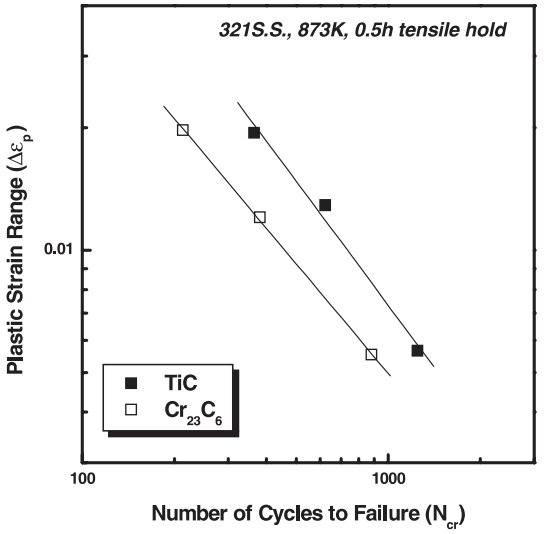

Fig. 7. Relationship between plastic strain range and the critical number of cycles for TiC and $Cr_{23}C_6$ aged AISI 321 stainless steel.

When the austenitic stainless steels are tested under creep–fatigue interaction conditions, the material fails due to the accumulation of a critical amount of grain boundary cavitation damage [7–13]. However, the creep–fatigue lives between TiC and $Cr_{23}C_6$ aged alloys show a remarkable difference in spite of the similar carbide density and morphology. It is suggested that the difference in creep–fatigue lives is related with the interfacial properties of the grain boundary carbides. In order to understand how TiC and $Cr_{23}C_6$ carbides affect creep–fatigue life, microstructural observations are discussed in the following section.

3.4. Grain boundary cavitation with TiC and $Cr_{23}C_6$ carbides during creep–fatigue interaction

At the critical fatigue life, the test was stopped and the specimen was fractured by impact at the LNT to investigate the possible damage under creep–fatigue condition. Fig. 8(a–c) and (b–d) show the fracture surfaces of TiC and $Cr_{23}C_6$ aged alloys, respectively. The two specimens show intergranular fracture modes at all the surfaces. For the TiC aged alloy, cavities and small dimples are observed in the fractured grain boundary as shown in Fig. 8(a) and (c). On the other hand, for $Cr_{23}C_6$ aged alloy, only cavities are observed, as shown in Fig. 8(b) and (d).

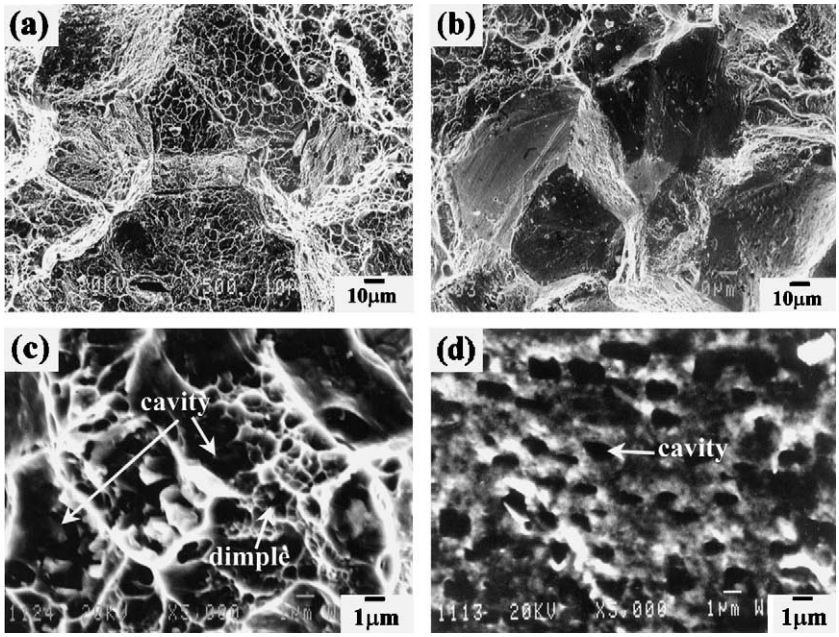

Fig. 8. SEM micrographs showing the fractured surfaces of TiC and $Cr_{23}C_6$ aged AISI 321 stainless steel by impact at LNT after creep–fatigue test ($T = 873$ K, $\Delta\varepsilon_t = \pm 1.0\%$, $t_h = 0.5$ h): (a) TiC, (b) $Cr_{23}C_6$, (c) high magnification of (a) and (d) high magnification of (b).

From the differences in fracture modes between TiC and $Cr_{23}C_6$ aged alloys, it is supposed that the different cavitation resistances of the alloys result from the interfacial characteristics of the TiC and $Cr_{23}C_6$ carbides. It is generally known that cavities are nucleated at carbides and geometrical irregularities with high interfacial free energy on grain boundaries where high tensile stress concentration can develop [9–11]. From the observation of the fractured surfaces in this investigation, it is supposed that the cavitation resistance of the TiC carbide interface is stronger than that of the $Cr_{23}C_6$ carbide interface.

When void is nucleated at a grain boundary, the expression for the total free energy is given by the following Eq. (1) [20].

$$\Delta F = -F_v r^3 \sigma_n \Omega + F_s \gamma_s r^2 - F_i \gamma_i r^2, \quad (1)$$

where r is the radii of void embryo, F_v, F_s and F_i are the volume factor, surface factor and interface factor, respectively, σ_n is applied tensile stress, Ω is atomic volume, γ_s is surface free energy and γ_i is interfacial free energy.

When a cavity is nucleated at a grain boundary carbide, the final term of Eq. (1) is changed such that

$$(F_{p/m}\gamma_s^p - F_{p/m}\gamma_{p/m} - F_b\gamma_b)r^2, \quad (2)$$

where F_b and $F_{p/m}$ are the grain boundary and interfacial area factor, and γ_s^p and $\gamma_{p/m}$ are surface free energy and interfacial free energy between the precipitate and matrix.

Using total free energy expressed by substituting Eqs. (2) into (1), when the interfacial free energy between a carbide and matrix has a lower value, the change of total free energy is lower. Therefore, nucleation of the void may be more difficult.

This is in good agreement with the results of creep–fatigue lives during creep–fatigue interaction. It is expected that stronger interfacial cohesion (lower interfacial free energy) between carbides and matrices will result in greater resistance to the formation and growth of cavities. As a result of the lower interfacial energy for TiC, the grain boundary cavitation at TiC carbides will be more delayed than that at $Cr_{23}C_6$ carbides.

4. Conclusions

1. The interfacial planes between TiC and neighboring grains show lower indices than those between $Cr_{23}C_6$ and neighboring grains. It is suggested that the interfacial free energy between TiC and grains is lower than that between $Cr_{23}C_6$ and grains in AISI 321 stainless steel. Also, the morphologies of carbides are determined by the minimization of interfacial free energy during the carbide growth.
2. Creep–fatigue life of TiC aged AISI 321 stainless steel is longer than that of $Cr_{23}C_6$ aged AISI 321 stainless steel. The differences in creep–fatigue life among the tested alloys are based on the strong cavitation resistance of TiC carbides compared with that of $Cr_{23}C_6$ carbides. From the interfacial relationships between carbides and neighboring grains, it is verified that formation and growth of grain boundary cavities at TiC carbides is slower than that at $Cr_{23}C_6$ carbides.

Acknowledgements

This research was sponsored by POSCO (Pohang Steel Making Co. Ltd.) as a project of BK21 (Brain Korea 21). The authors would like to express their appreciation for the financial support.

References

[1] J.H. Payer, R.W. Staehle, Corrosion 31 (1975) 30.
[2] C. Hoffmann, A.J. Mccevily, Metall. Trans. A 13 (1982) 923.
[3] M. Schwind, J. Källqvist, J.-O. Nilsson, J. Ågren, H.-O. Andrén, Acta Mater. 48 (2000) 2473.
[4] A.S. Grot, J.E. Spruiell, Metall. Trans. A 6 (1975) 2023.
[5] T. Thorvaldsson, G.L. Dunlop, Met. Sci. (1980) 513.
[6] J.K.L. Lai, Mater. Sci. Tech. 1 (1985) 97.
[7] P.S. Maiya, S. Majumdar, Metall. Trans. A 8 (1977) 1651.
[8] M.H. Yoo, H. Trinkaus, Metall. Trans. A 14 (1983) 547.
[9] J.W. Hong, S.W. Nam, K.-T. Rie, J. Mater. Sci. 20 (1985) 3763.
[10] B.G. Choi, S.W. Nam, Y.C. Yoon, J.J. Kim, J. Mater. Sci. 31 (1996) 4957.
[11] S.W. Nam, Y.C. Yoon, B.G. Choi, J.M. Lee, J.W. Hong, Metall. Mater. Trans. A 27 (1996) 1273.
[12] S.W. Nam, Mater. Sci. Eng. A 322 (2002) 64.
[13] J.M. Lee, S.W. Nam, Int. J. Damage. Mech. 2 (1993) 4.
[14] H.U. Hong, B.S. Rho, S.W. Nam, Mater. Sci. Eng. A 318 (2001) 285.
[15] T. Furuhara, S. Takagi, H. Watanabe, T. Maki, Metall. Mater. Trans. A 27 (1996) 1635.
[16] K.-T. Rie, H.P. Stüwe, Z. Metallkd. 64 (1973) 37.
[17] W. Lojkowski, H. Gleiter, R. Maurer, Acta Metall. 36 (1988) 69.
[18] S. Hirth, G. Gottstein, Acta Mater. 46 (1998) 3975.
[19] H.U. Hong, S.W. Nam, Mater. Sci. Eng. A 332 (2002) 255.
[20] R. Raj, M.F. Ashby, Acta Metall. 23 (1975) 653.